International Journal of Solids and Structures 51 (2014) 3715–3726

Contents lists available at ScienceDirect

International Journal of Solids and Structures

journal homepage: www.elsevier.com/locate/ijsolstr

Nonlinear analysis of compressed elastic thin films on elastic substrates: From wrinkling to buckle-delamination

Kui Pan [a], Yong Ni [a,*], Linghui He [a], Rui Huang [b,*]

[a] CAS Key Laboratory of Mechanical Behavior and Design of Materials, and Department of Modern Mechanics, University of Science and Technology of China, Hefei, Anhui 230026, PR China

[b] Department of Aerospace Engineering and Engineering Mechanics, University of Texas, Austin, TX 78712, USA

ARTICLE INFO

Article history:
Received 3 December 2013
Received in revised form 8 July 2014
Available online 23 July 2014

Keywords:
Thin film
Buckling
Delamination
Interface

ABSTRACT

Nonlinear buckling of elastic thin films on compliant substrates is studied by modeling and simulations to reveal the roles of pre-strain, elastic modulus ratio, and interfacial properties in morphological transition from wrinkles to buckle-delamination blisters. The model integrates an interfacial cohesive zone model with the Föppl–von Kármán plate theory and Green function method within the general framework of energy minimization. A kinetics approach is developed for numerical simulations. Subject to a uniaxial pre-strain, the numerical simulations confirm the analytically predicted critical conditions for onset of wrinkling and wrinkle-induced delamination, with which a phase diagram is constructed. It is found that, with increasing pre-strain, the equilibrium configuration evolves from flat to wrinkles, to concomitant wrinkles and buckle-delamination, and to an array of parallel straight blisters. The height and width of the buckle-delamination blisters can be approximately described by a set of scaling laws with respect to the pre-strain and interfacial toughness. Subject to an equi-biaxial pre-strain, the critical conditions are determined numerically to construct a similar phase diagram for the buckling modes. Moreover, by varying the pre-strain, modulus ratio, and interfacial toughness, a rich variety of equilibrium configurations are simulated, including straight blisters, and network blisters with or without wrinkles. These results provide considerable insight into diverse surface patterns in layered material systems as a result of the mechanical interactions between the film and the substrate through their interface, which suggests potential control parameters for designing specific surface patterns.

1. Introduction

Thin film materials are widely used in advanced technologies (Hutchinson and Suo, 1992; Freund and Suresh, 2003). When a thin film is under in-plane compression, it often leads to formation of surface wrinkles or buckle-delamination blisters as a result of buckling instability. Understanding the thin film surface morphology is important in various applications, such as flexible electronics (Lacour et al., 2005; Khang et al., 2006), surface coating (Evans et al., 2001), thin film metrology (Stafford et al., 2004; Vella et al., 2009), and surface patterning (Genzer and Groenewold, 2006). On a relatively compliant substrate, wrinkling is typically observed (Bowden et al., 1998; Yoo et al.,2002; Ohzono and Shimomura, 2004; Efimenko et al., 2005; Vandeparre and Damman, 2008; Yang et al., 2010). On a relatively stiff substrate, buckle-delamination blisters are more likely to occur (Gioia and Ortiz, 1997; Moon et al., 2002; Parry et al., 2006; Abdallah et al., 2006; Vella et al., 2009; Faou et al., 2012). In some thin film systems, wrinkles and buckle-delamination blisters can co-exist and co-evolve (Mei et al., 2007; Goyal et al., 2010). The polymorphism of the buckling morphology reflects the rich mechanics of nonlinear buckling in the thin film and layered material systems. While both wrinkling and buckle-delamination have been studied extensively, it remains unclear how the buckling morphology evolves, especially when both wrinkling and buckle-delamination are theoretically possible.

Most of the previous studies have considered wrinkling and buckle-delamination separately. Assuming no delamination, the critical condition for onset of wrinkling can be predicted by a linear perturbation analysis, while the equilibrium wrinkle wavelength and amplitude are predicted via an energetic analysis (Groenewold, 2001; Chen and Hutchinson, 2004; Huang, 2005; Huang et al., 2005; Jiang et al., 2007; Audoly and Boudaoud, 2008; Cai et al., 2011). A variety of wrinkling patterns have been predicted or simulated by analytic and numerical calculations based on the principle of energy minimization (Chen and Hutchinson, 2004; Huang et al., 2004, 2005; Peyla, 2005; Huang

* Corresponding authors.
E-mail addresses: yni@ustc.edu.cn (Y. Ni), ruihuang@mail.utexas.edu (R. Huang).

http://dx.doi.org/10.1016/j.ijsolstr.2014.07.005
0020-7683/

and Im, 2006; Cao et al., 2008; Im and Huang, 2008; Audoly and Boudaoud, 2008; Uchida and Ohzono, 2010; Cai et al., 2011; Ni et al., 2011). On the other hand, pre-existing interfacial delamination is commonly assumed in the studies of buckle-delamination blisters, which have largely focused on the growth of buckle-delamination blisters (Chai et al., 1981; Hutchinson et al., 1992; Ortiz and Gioia, 1994; Nilsson and Giannakopoulos, 1995; Audoly, 1999; Jagla, 2007). Recently, it was found that the critical condition for onset of buckling depends sensitively on the pre-existing delamination, and a smooth transition from buckle-delamination to wrinkling with decreasing delamination size was predicted by a finite element eigenvalue analysis (Mei et al., 2011). Without pre-existing delamination, progressive wrinkling with increasing amplitude may lead to nucleation of interfacial delamination and subsequently co-evolution of wrinkles and buckle-delamination blisters (Goyal et al., 2010; Mei et al., 2011). In this paper we present a unified modeling approach to simulate morphological evolution from wrinkling to buckle-delamination for elastic thin films on elastic substrates, which can be used to systematically study the roles of pre-strain, film/substrate modulus ratio, and the interfacial properties.

The remainder of this paper is organized as follows. In Section 2, we present a theoretical model that integrates the Föppl–von Kármán (FvK) plate theory for the film, the Green function method for the substrate, and a cohesive zone model for the interface. In Section 3, a numerical method based on a kinetics approach is described. Section 4 presents the results from numerical simulations under uniaxial and equi-biaxial compression, in comparison with previously reported analytical predictions and scaling analysis. A variety of post-buckling morphology is simulated as a result of the interplay between wrinkling and buckle-delamination. Section 5 concludes the present study with a brief summary.

2. Theoretical model

Consider an elastic thin film of thickness h bonded onto an elastic substrate; the substrate is assumed to be of infinite thickness in the present study. Under in-plane compression, the film tends to buckle. As shown in Fig. 1, surface wrinkling (without interfacial delamination) and buckle-delamination are two typical buckling modes. In this section, a theoretical model is developed to study both buckling modes and their interactions in a unified framework. We model the film as an isotropic FvK plate with a prestrain, the semi-infinite substrate by a Green function method, and the film/substrate interface by a cohesive zone model, described as follows.

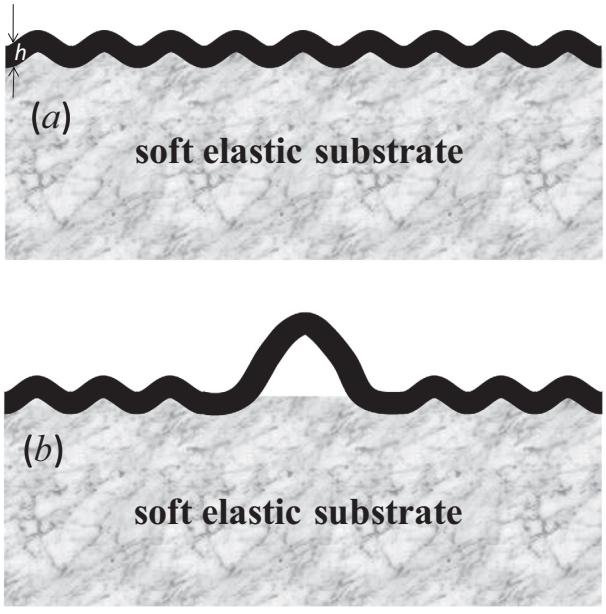

Fig. 1. Schematic illustration of (a) wrinkling and (b) wrinkle-induced delamination in an elastic film on an elastic substrate.

2.1. Deformation and energetics of an elastic film

Consider an elastic film with an in-plane eigenstrain, $\varepsilon^0_{\alpha\beta}$, which may result from thermal expansion, solvent absorption induced swelling, or volume change by microstructural transformation. Constrained by the substrate, the total in-plane strain in the film consists of the prescribed eigenstrain (or prestrain) and the strain due to elastic deformation, $\varepsilon^{el}_{\alpha\beta}$. Under the assumption of small strain, the total strain is simply the sum of the two parts:

$$\varepsilon^{tot}_{\alpha\beta} = \varepsilon^0_{\alpha\beta} + \varepsilon^{el}_{\alpha\beta}, \tag{2.1}$$

which is defined with respect to a stress-free reference state before imposing the eigenstrain.

According to the FvK plate theory (Mansfield, 1989), the displacement components at any point in the film, $\bar{u}_i$ ($i = 1$–3), can be expressed by the middle-plane displacement, $\mathbf{u} = (u_\alpha, \zeta)$, based on the Kirchhoff assumption:

$$\begin{aligned} &\bar{u}_\alpha = u_\alpha - x_3\zeta_{,\alpha}, \qquad (\alpha = 1,2) \\ &\bar{u}_3 = \zeta(x_1, x_2). \end{aligned} \tag{2.2}$$

The total in-plane strain is then

$$\varepsilon^{tot}_{\alpha\beta} = \frac{1}{2}(\bar{u}_{\alpha,\beta} + \bar{u}_{\beta,\alpha}) + \frac{1}{2}\bar{u}_{3,\alpha}\bar{u}_{3,\beta}, \tag{2.3}$$

where a nonlinear term is included to account for geometrical nonlinearity due to moderately large deflection of the elastic film. The Greek indices are used for in-plane coordinates 1 or 2, and Latin indices for 1, 2 or 3. The usual summation convention applies for repeated indices, and a comma stands for differentiation with respect to the suffix index.

Substituting Eqs. (2.2) and (2.3) into (2.1), the elastic strain in the thin film is obtained as

$$\varepsilon^{el}_{\alpha\beta} = e_{\alpha\beta} - x_3\zeta_{,\alpha\beta}, \tag{2.4}$$

where

$$e_{\alpha\beta} = \frac{1}{2}(u_{\alpha,\beta} + u_{\beta,\alpha}) + \frac{1}{2}\zeta_{,\alpha}\zeta_{,\beta} - \varepsilon^0_{\alpha\beta} \tag{2.5}$$

is the elastic membrane strain of the film at the mid-plane ($x_3 = 0$).

The stress in the film is related to the elastic strain as

$$\sigma^{el}_{\alpha\beta} = \frac{2\mu_f}{1-\nu_f}[(1-\nu_f)\varepsilon^{el}_{\alpha\beta} + \nu_f\varepsilon^{el}_{\gamma\gamma}\delta_{\alpha\beta}], \tag{2.6}$$

where μ_f and ν_f are the shear modulus and Poison ratio of the film, respectively.

The total elastic strain energy in the film is obtained by integrating through its volume, namely

$$U^{film} = \int_{-h/2}^{h/2}\int_{-\infty}^{\infty}\int_{-\infty}^{\infty}\frac{1}{2}\sigma^{el}_{\alpha\beta}\varepsilon^{el}_{\alpha\beta}dx_1dx_2dx_3. \tag{2.7}$$

Substituting Eqs. (2.4)–(2.6) into (2.7) and integrating with respect to x_3 leads to

$$U^{film} = U^{film}_s + U^{film}_b, \tag{2.8}$$

where U^{film}_s and U^{film}_b are the stretching energy and the bending energy in the film, respectively, defined as follows:

$$U^{film}_s = \frac{1}{2}\int_{-\infty}^{\infty}\int_{-\infty}^{\infty}N_{\alpha\beta}e_{\alpha\beta}dx_1dx_2, \tag{2.9}$$

$$U_b^{film}=\frac{\mu_f h^3}{12(1-\nu_f)}\int_{-\infty}^{\infty}\int_{-\infty}^{\infty}\{(\Delta\zeta)^2-2(1-\nu_f)[\zeta_{,11}\zeta_{,22}-(\zeta_{,12})^2]\}dx_1dx_2. \tag{2.10}$$

In Eq. (2.9), the membrane force $N_{\alpha\beta}$ is obtained by integrating the stress in (2.6) with respect to the film thickness, which consists of three parts, namely

$$N_{\alpha\beta}=N_{\alpha\beta}^{(0)}+N_{\alpha\beta}^{(1)}+N_{\alpha\beta}^{(2)}, \tag{2.11}$$

with

$$N_{\alpha\beta}^{(0)}=-\frac{2h\mu_f}{1-\nu_f}[(1-\nu_f)\varepsilon_{\alpha\beta}^0+\nu_f\varepsilon_{\gamma\gamma}^0\delta_{\alpha\beta}], \tag{2.12}$$

$$N_{\alpha\beta}^{(1)}=\frac{h\mu_f}{1-\nu_f}[(1-\nu_f)(u_{\alpha,\beta}+u_{\beta,\alpha})+2\nu_f u_{\gamma,\gamma}\delta_{\alpha\beta}], \tag{2.13}$$

$$N_{\alpha\beta}^{(2)}=\frac{h\mu_f}{1-\nu_f}[(1-\nu_f)\zeta_{,\alpha}\zeta_{,\beta}+\nu_f\zeta_{,\gamma}\zeta_{,\gamma}\delta_{\alpha\beta}]. \tag{2.14}$$

Note that the effect of eigenstrain is incorporated in the membrane force, in addition to the linear and nonlinear parts resulting from the in-plane and out-of-plane displacements, respectively. Furthermore, a positive eigenstrain (uniaxial or equi-biaxial) results in a compressive membrane force $N_{\alpha\beta}^{(0)}$ in the film, which is the driving force for the buckling deformation.

2.2. Deformation and energetics of an elastic substrate

The semi-infinite substrate is subject to surface tractions via the interaction with the film. The elastic strain energy of the substrate can be written as a surface integral

$$U^{sub}=\frac{1}{2}\int_{-\infty}^{\infty}\int_{-\infty}^{\infty}T_i^s u_i^s dx_1dx_2, \tag{2.15}$$

where T_i^s, u_i^s are the traction and displacement components on the substrate surface. By the Green function method, the surface traction, T_i^s is expressed as a function of the surface displacement, u_i^s for a semi-infinite elastic substrate with shear modulus μ_s and Poisson ratio ν_s (Huang et al., 2005)

$$T_i^s=\frac{1}{(2\pi)^2}\int\int M_{ij}\tilde{u}_j^s e^{i\xi_\alpha x_\alpha}d\xi_1d\xi_2, \tag{2.16}$$

where ξ_α is the component of the Fourier vector, and M_{ij} is defined as the inverse of the surface Green function of the half space in the Fourier space

$$M_{ij}=\frac{\mu_s\xi}{3-4\nu_s}\begin{bmatrix}4(1-\nu_s)-n_2^2 & n_1n_2 & 2i(1-2\nu_s)n_1\\ n_1n_2 & 4(1-\nu_s)-n_1^2 & 2i(1-2\nu_s)n_2\\ -2i(1-2\nu_s)n_1 & -2i(1-2\nu_s)n_2 & 4(1-\nu_s)\end{bmatrix}, \tag{2.17}$$

with

$$\xi=(\xi_1^2+\xi_2^2)^{1/2},\quad n_1=\xi_1/\xi,\quad n_2=\xi_2/\xi, \tag{2.18}$$

and $\tilde{u}_j^s$ is the Fourier transform of u_j^s

$$\tilde{u}_j^s(\xi)=\int_{-\infty}^{\infty}\int_{-\infty}^{\infty}u_j^s(x_1,x_2)e^{-i(\xi_1x_1+\xi_2x_2)}dx_1dx_2. \tag{2.19}$$

Throughout the paper, the tilt over a symbol denotes its Fourier transform. Fourier transform of Eq. (2.16) leads to: $\tilde{T}_i^s=M_{ij}\tilde{u}_j^s$.

2.3. A cohesive zone model for interface

A cohesive zone model is adopted for the interface between the film and the substrate, in which the interfacial property is represented by a nonlinear traction-separation relation derived from a potential energy function (Xu and Needleman, 1994). Denote the displacement jump across the interface as $\mathbf{\Lambda}$, and the potential energy of the interface as $\phi(\mathbf{\Lambda})$. The interfacial traction is then obtained as $\mathbf{T}=\partial\phi(\mathbf{\Lambda})/\partial\mathbf{\Lambda}$. In the present study, a specific form of the potential energy function with mixed-mode decohesion (van den Bosch et al., 2006; Park et al., 2009) is used, in which the adhesion energy depends on the decohesion path as a functional of $\mathbf{\Lambda}$ and the interfacial traction components are obtained as

$$T_3=\frac{\gamma_n\Lambda_n}{\delta_n^2}\exp\left(-\frac{\Lambda_n}{\delta_n}-\frac{\Lambda_t^2}{\delta_t^2}\right), \tag{2.20}$$

$$T_\alpha=\frac{2\gamma_t\Lambda_\alpha}{\delta_t^2}\left(1+\frac{\Lambda_n}{\delta_n}\right)\exp\left(-\frac{\Lambda_n}{\delta_n}-\frac{\Lambda_t^2}{\delta_t^2}\right), \tag{2.21}$$

where $\Lambda_n=\Lambda_3$ and $\Lambda_t=\sqrt{\Lambda_1^2+\Lambda_2^2}$ are the normal and tangential components of the displacement jump across the interface, respectively. Four parameters are needed in the cohesive zone model: γ_n and γ_t are the normal and tangential interfacial toughness, respectively; δ_n and δ_t are two characteristic lengths corresponding to the normal and tangential displacement jump. In particular, with $\Lambda_t=0$ (pure mode I), the normal traction given by Eq. (2.20) reaches a maximum value, $\sigma_{\max}=\frac{\gamma_n}{e\delta_n}$, at $\Lambda_n=\delta_n$. With $\Lambda_n=0$ (pure mode II), the shear traction given by Eq. (2.21) reaches a maximum value, $\tau_{\max}=\frac{\gamma_t}{\delta_t}\sqrt{\frac{2}{e}}$, at $\Lambda_t=\delta_t/\sqrt{2}$. The maximum tractions, $\sigma_{\max}$ and $\tau_{\max}$, are often called the normal and tangential strengths of the interface, respectively. Under a mixed mode condition, however, the traction-separation relations depend on the mode mix, which may be defined by the ratio between the traction components, T_α/T_n, or the ratio between the displacement components, Λ_α/Λ_n. It can be shown that the interfacial fracture toughness, obtained by integrating the traction-separation relations, $\gamma=\int_0^\infty T_n d\Lambda_n+\int_0^\infty T_\alpha d\Lambda_\alpha$, is independent of mode mix if $\gamma_n=\gamma_t$. When $\gamma_n\neq\gamma_t$, the fracture toughness is in between, $[\gamma_n,\gamma_t]_{\min}\leqslant\gamma\leqslant[\gamma_n,\gamma_t]_{\max}$, depending on the mode mix. We note that $\Lambda_n<0$ leads to apparently unphysical inter-penetration in the current cohesive zone model. A small inter-penetration can be accommodated if a nonzero equilibrium gap between the film and the substrate due to their intermolecular forces is taken into account. Alternatively, a consistent cohesive zone model can be constructed using the concept of deformation-coupled intermolecular interaction between two bodies (He, 2013).

The displacement jump across the interface is related to the displacements of the film and the substrate surface by the geometric conditions as

$$\begin{aligned}\Lambda_3&=\zeta-u_3^s\\ \Lambda_\alpha&=u_\alpha+\frac{h}{2}\zeta_{,\alpha}-u_\alpha^s.\end{aligned} \tag{2.22}$$

2.4. A variational analysis

The equilibrium configuration is obtained by minimizing the total energy of the material system including the film, the substrate, and the interface:

$$U^{tot}=U^{film}+U^{sub}+\int_{-\infty}^{\infty}\int_{-\infty}^{\infty}\phi(\Lambda)dx_1dx_2 \tag{2.23}$$

With the geometric conditions in (2.22), the total energy is taken to be a function of the film displacements (u_α and ζ) and the interfacial separation (Λ_α and Λ_3). At the equilibrium state, the variations of U^{tot} with respect to u_α, Λ_α, ζ and Λ_3 vanish. Specifically, $\delta U^{tot}/\delta\Lambda_3 = 0$ leads to the normal traction continuity relation

$$T_3 - T_3^s = 0, \tag{2.24}$$

Similarly, $\delta U^{tot}/\delta\Lambda_\alpha = 0$ leads to the tangential traction continuity relation

$$T_\alpha - T_\alpha^s = 0. \tag{2.25}$$

Furthermore, $\delta U^{tot}/\delta\zeta = 0$ recovers the equilibrium equation for the film in the normal direction

$$D\Delta^2\zeta - (N_{\alpha\beta}\zeta_{,\alpha})_{,\beta} + T_3^s - \frac{h}{2}T_{\alpha,\alpha}^s = 0, \tag{2.26}$$

where $D = \mu_f h^3/6(1-\nu_f)$ is the bending rigidity of the film.

Finally, $\delta U^{tot}/\delta u_\alpha = 0$ reduces to the in-plane equilibrium equation for the film:

$$N_{\alpha\beta,\beta} = T_\alpha^s. \tag{2.27}$$

With Eqs. (2.11)–(2.14), Eq. (2.27) can be written in the Fourier space as

$$C_{\alpha\beta}\tilde{u}_\beta = \tilde{\rho}_\alpha, \tag{2.28}$$

where

$$C_{\alpha\beta} = (h\mu_f\xi^2 + \mu_s\xi)\delta_{\alpha\beta} + \left[\frac{h\mu_f}{1-\nu_f}(1+\nu_f)\xi^2 + \frac{\mu_s}{3-4\nu_s}\xi\right]n_\alpha n_\beta, \tag{2.29}$$

$$\tilde{\rho}_\alpha = i\xi n_\beta(\tilde{N}_{\alpha\beta}^{(0)} + \tilde{N}_{\alpha\beta}^{(2)}) + M_{\alpha\beta}\tilde{\Lambda}_\beta + M_{\alpha3}(\tilde{\Lambda}_3 - \tilde{\zeta}). \tag{2.30}$$

With Eq. (2.28), the in-plane elastic strain of the film in Eq. (2.5) can be written explicitly in form of Green function, namely

$$e_{\alpha\beta}(x_1,x_2) = \frac{1}{2}\int_{|\xi|\neq0}\frac{i(\xi_\alpha\tilde{G}_{\beta k} + \xi_\beta\tilde{G}_{\alpha k})\tilde{\rho}_k e^{i\xi\cdot\mathbf{r}}}{(2\pi)^2}d^2\xi + \frac{1}{2}\zeta_{,\alpha}\zeta_{,\beta} - \varepsilon_{\alpha\beta}^0, \tag{2.31}$$

where $\tilde{G}_{\alpha\beta}$ is the Green function in the Fourier space defined as the inverse of $C_{\alpha\beta}$:

$$\tilde{G}_{\alpha\beta} = \frac{\delta_{\alpha\beta}}{h\mu_f\xi^2 + \mu_s\xi} - \frac{\left[h\mu_f\xi^2\frac{(1+\nu_f)}{(1-\nu_f)} + \frac{\mu_s\xi}{(3-4\nu_s)}\right]n_\alpha n_\beta}{(h\mu_f\xi^2 + \mu_s\xi)\left[\frac{2h\mu_f\xi^2}{(1-\nu_f)} + \frac{4(1-\nu_s)\mu_s\xi}{(3-4\nu_s)}\right]}. \tag{2.32}$$

In general, by solving Eqs. (2.24)–(2.27), we obtain six field quantities in the two-dimensional space (x_1, x_2): ζ, u_α, Λ_3 and Λ_α. By Eq. (2.28), the Fourier transform of u_α can be solved for given ζ, Λ_3 and Λ_α, thus reducing the number of unknowns to four. An iterative procedure may be used to solve these nonlinear equations numerically. Alternatively, a kinetics approach is developed to solve the nonlinear system, as presented in Section 3.

3. Numerical method: a kinetics approach

Instead of directly solving the coupled nonlinear equations in (2.24)–(2.26) for the equilibrium configuration, we consider a set of Ginzburg–Landau kinetic equations (Carter et al., 1997):

$$\frac{\partial\zeta}{\partial t} = -\Gamma_\zeta\frac{\delta U^{tot}}{\delta\zeta}, \tag{3.1}$$

$$\frac{\partial\Lambda_3}{\partial t} = -\Gamma_{\Lambda_3}\frac{\delta U^{tot}}{\delta\Lambda_3}, \tag{3.2}$$

$$\frac{\partial\Lambda_\alpha}{\partial t} = -\Gamma_{\Lambda_\alpha}\frac{\delta U^{tot}}{\delta\Lambda_\alpha}, \tag{3.3}$$

where Γ_ζ, Γ_{Λ_3}, and Γ_{Λ_α} are kinetic coefficients characterizing the relaxation rates of the buckling and delamination processes, respectively, assuming an over-damped dynamic system. Apparently, solving Eqs. (3.1)–(3.3) gives the time evolution of the field quantities. After a sufficiently long time, the system may approach a steady-state ($\partial/\partial t = 0$), which gives the equilibrium configuration equivalent to the solutions of Eqs. (2.24)–(2.26). One may consider the kinetic equations in (3.1)–(3.3) representing a dissipative process through which the field quantities evolve to reduce the total energy in the system until it reaches the steady state.

Inserting (2.23) as the total energy into (3.1)–(3.3), we obtain

$$\frac{\partial\zeta}{\partial t} = -\Gamma_\zeta\left[D\Delta^2\zeta - (N_{\alpha\beta}\zeta_{,\alpha})_{,\beta} + T_3^s - \frac{h}{2}T_{\alpha,\alpha}^s\right], \tag{3.4}$$

$$\frac{\partial\Lambda_3}{\partial t} = -\Gamma_{\Lambda_3}(T_3 - T_3^s), \tag{3.5}$$

$$\frac{\partial\Lambda_\alpha}{\partial t} = -\Gamma_{\Lambda_\alpha}(T_\alpha - T_\alpha^s). \tag{3.6}$$

where the tractions are obtained from (2.16), (2.20) and (2.21), and the in-plane displacement of the film is obtained from (2.28). Therefore, by solving the coupled kinetic equations (3.4)–(3.6) numerically, we can simulate nonlinear evolution of both buckling and delamination of the elastic thin film.

A spectral method is employed in the present study for numerical simulations. Briefly, Fourier transform of Eqs. (3.4)–(3.6) leads to

$$\frac{\partial\tilde{\zeta}}{\partial t} = -\Gamma_\zeta\begin{bmatrix}\left(D\xi^4 + M_{33} + i\xi hM_{3\beta}n_\beta + \frac{1}{4}\xi^2h^2M_{\alpha\beta}n_\alpha n_\beta\right)\tilde{\zeta} - i\xi n_\beta\tilde{P}_\beta \\ +\left(M_{3\beta} - \frac{i}{2}\xi hM_{\alpha\beta}n_\alpha\right)(\tilde{u}_\beta - \tilde{\Lambda}_\beta) - \left(M_{33} - \frac{i}{2}\xi hM_{\alpha3}n_\alpha\right)\tilde{\Lambda}_3\end{bmatrix} \tag{3.7}$$

$$\frac{\partial\tilde{\Lambda}_3}{\partial t} = -\Gamma_3\left[\tilde{T}_3 - \left(M_{33} + \frac{i}{2}\xi hM_{3\beta}n_\beta\right)\tilde{\zeta} + M_{33}\tilde{\Lambda}_3 - M_{3\beta}(\tilde{u}_\beta - \tilde{\Lambda}_\beta)\right] \tag{3.8}$$

$$\frac{\partial\tilde{\Lambda}_\alpha}{\partial t} = -\Gamma_\alpha\left[\tilde{T}_\alpha - \left(M_{\alpha3} + \frac{i}{2}\xi hM_{\alpha\beta}n_\beta\right)\tilde{\zeta} + M_{\alpha3}\tilde{\Lambda}_3 - M_{\alpha\beta}(\tilde{u}_\beta - \tilde{\Lambda}_\beta)\right] \tag{3.9}$$

where $P_\beta = N_{\alpha\beta}\zeta_{,\alpha}$. Note that the right-hand side of Eqs. (3.7)–(3.9) includes both linear and nonlinear terms. A semi-implicit algorithm is then adopted to integrate these equations over time, similar to that in a previous study (Huang and Im, 2006).

In the numerical simulations, the dimensional quantities are normalized by scaling the length with the film thickness and the time with $\tau = h/\Gamma_\zeta\mu_s$ (i.e., $t' = t/\tau$). Square computational domains of size 1024×1024 are used with periodical boundary conditions and the time step $\Delta t' = 1$. A randomly generated small fluctuation of ζ is introduced throughout the simulations to mimic thermal fluctuation that facilitates onset of buckling and nucleation of buckle-delamination. In the present study, we consider homogeneous pre-strains, with uniaxial and equi-biaxial components. We focus our study on the effects of the modulus ratio μ_f/μ_s and the interfacial toughness, normalized by $\gamma^* = h\mu_s$. For simplicity, the interfacial toughness is assumed to be independent of the mixed mode, $\gamma = \gamma_t = \gamma_n$ (unless noted otherwise). To be specific, we have used the following parameters in our simulations: $\nu_f = 0.3$, $\delta_n/h = \delta_t/h = 0.2$ such that the time step can be large enough and the calculated post-buckling profile is not sensitive to the variation of $\delta_n/h, \delta_t/h$ in the case of fixing the value of the

interfacial toughness, γ_t, γ_n. And $\Gamma_{\Lambda_3}/\Gamma_\zeta = \Gamma_{\Lambda_\alpha}/\Gamma_\zeta = 0.002$ guarantee that the delamination process is usually much slower than that of the buckling process. By the way the equilibrium buckling profile is not sensitive to the variation of $\Gamma_{\Lambda_i}/\Gamma_\zeta$ as we have checked. Moreover, we have taken the substrate to be incompressible ($\nu_s = 0.5$) so that the matrix M_{ij} in (2.17) is greatly simplified.

4. Results and discussions

4.1. Initiation of wrinkling-induced delamination under uniaxial compression

Start from a flat configuration of the film/substrate system with a perfect interface. Subject to uniaxial in-plane compression, the critical strain for the onset of wrinkling instability is (Chen and Hutchinson, 2004; Huang et al., 2005)

$$\varepsilon_w = \frac{1}{4}\left(\frac{3\mu_s(1-\nu_f)}{\mu_f(1-\nu_s)}\right)^{2/3} \tag{4.1}$$

Beyond the critical strain, the wrinkle amplitude grows, inducing normal and shear tractions along the interface. The critical strain to cause initiation of interfacial delamination was predicted by Mei et al. (2011) as

$$\varepsilon_{wd} = \varepsilon_w + \left[\frac{(3-4\nu_s)\sigma_{\max}}{8(1-\nu_s)\mu_s}\right]^2 \tag{4.2}$$

where $\sigma_{\max}$ is the interfacial strength in the normal direction. By the cohesive zone model in Section 2.3, the interfacial strength is related to the interfacial toughness as $\sigma_{\max} = \frac{\gamma_n}{e\delta_n}$.

With the two critical strains, we construct a phase diagram for the morphology of the film/substrate system, as shown in Fig. 2. The pre-strain is scaled by the critical strain for wrinkling, and the interfacial properties as well as the elastic mismatch are lumped into one dimensionless parameter, $q = \frac{3-4\nu_s}{4e(1-\nu_s)}\left(\frac{\mu_f(1-\nu_s)}{3\mu_s(1-\nu_f)}\right)^{1/3}\left(\frac{\gamma_n}{\mu_s\delta_n}\right)$. In this way, the critical condition for wrinkling is represented by one horizontal line in the panel, and the critical condition for initiation of wrinkling induced delamination is a single curve, $\frac{\varepsilon_{wd}}{\varepsilon_w} = 1+q^2$. Therefore, the panel in Fig. 2 is divided into three regions for flat (I), wrinkling with no delamination (II), and wrinkle-induced delamination (III). By using the present model and numerical simulations without imposing any ad hoc constraints on the buckling mode, we determined the critical conditions for the transitions from flat to wrinkling and to wrinkle-induced delamination by tracking the field variables ζ, Λ_3 and Λ_α in the film/substrate system subject to increasing prestrain, ε_{pre}, for various combinations of the modulus ratio, μ_f/μ_s, and normalized interface toughness, $\gamma/(\mu_s h)$. For example, the transition from flat to wrinkling is taken approximately when the root-mean-square (RMS) average of the deflection is larger than a critical value, i.e. $\bar{\zeta} = \sqrt{\langle\zeta^2\rangle} > 0.01h$, while the interfacial separation remains small ($|\Lambda_3|_{\max} < \delta_n$); the transition from wrinkling to wrinkle-induced delamination occurs when the maximum interfacial separation becomes large enough so that the corresponding interfacial traction is nearly zero, i.e., $|\Lambda_3|_{\max} > 4\delta_n$. As shown in Fig. 2, the critical strains determined numerically for various material parameters collapse onto the two lines predicted by (4.1) and (4.2).

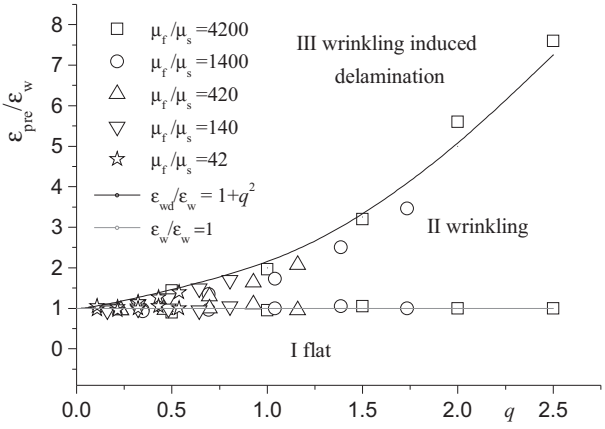

Fig. 2. A phase diagram for wrinkling and delamination in the elastic film/substrate systems under uniaxial compression. The solid lines are the theoretically predicted critical strains, and the open symbols are the critical strains obtained by numerical simulations with various modulus ratios.

Fig. 3 shows the results from two representative numerical simulations, both under a uniaxial compression with the eigenstrain $\varepsilon_{pre} = 0.003$. With the elastic modulus ratio $\mu_f/\mu_s = 4200$, the critical strain for onset of wrinkling by Eq. (4.1) is $\varepsilon_w = 0.0025$. For the case of a high interfacial toughness ($\gamma_n/\gamma^* = 2.7$), the critical strain for wrinkle-induced delamination is $\varepsilon_{wd} = 1.56$ by Eq. (4.2). Thus, the eigenstrain is sufficient to cause wrinkling, but not delamination. Indeed, the numerical simulation shows periodic wrinkles of the film with the normalized deflection (ζ/h) in Fig. 3(a) while the normal displacement jump (Λ_3/h) across the interface remains nearly zero indicating no delamination. On the other hand, for the case of a low interfacial toughness ($\gamma_n/\gamma^* = 0.005$), $\varepsilon_{wd} = 0.002506$, and the eigenstrain is sufficient to cause wrinkling and delamination. In this case, the numerical simulation shows the film deflection (ζ/h) and the displacement jump (Λ_3/h) across the interface evolve simultaneously in Fig. 3(b)–(d). At the initial stage (Fig. 3(b)), the film wrinkles periodically, and the normal displacement jump is relatively small ($\Lambda_3 < \delta_n$) and hence no delamination. As shown in Fig. 3(c), with increasing wrinkle amplitude, the displacement jump (Λ_3) increases and reaches a critical point for nucleation of delamination. It is found that the delamination typically nucleates underneath one of the wrinkle peaks, while the exact location depends on the random fluctuation in the numerical simulations. Subsequently, as the delamination grows, the wrinkled configuration gradually transforms into localized buckle-delamination. Eventually, an equilibrium configuration is reached, with a straight buckle-delamination blister in the computational domain. We note that this equilibrium configuration in general depends on the computational domain size due to the periodic boundary conditions used in the numerical simulation.

4.2. Growth of wrinkle-induced delamination under uniaxial compression

The growth of wrinkles and wrinkle-induced delamination is driven by a configurational force to minimize the total energy in the film-substrate system. Fig. 4 plots the energy changes during evolution of wrinkling and buckle-delamination presented in Fig. 3. For the case of pure wrinkling, Fig. 4(a) shows that the decrease of the stretch energy in the film is accompanied by the increase of bending energy in the film and elastic energy in the substrate when the wrinkle amplitude starts growing rapidly at $t' > 8\times10^3$, while the potential energy of the interface remains negligible. As a result, the total energy decreases. As the wrinkles evolve towards the equilibrium state, the energy approaches a plateau. The equilibrium wrinkle amplitude and wavelength compare closely with analytical solutions. For the case of wrinkling-induced delamination, Fig. 4(b) shows that the energy relaxation has three distinctive stages. The first stage is due to the wrinkle formation and growth from $t' \sim 8\times10^3$ to $t' \sim 4\times10^4$, when the potential energy of the interface is relatively small compared to the other

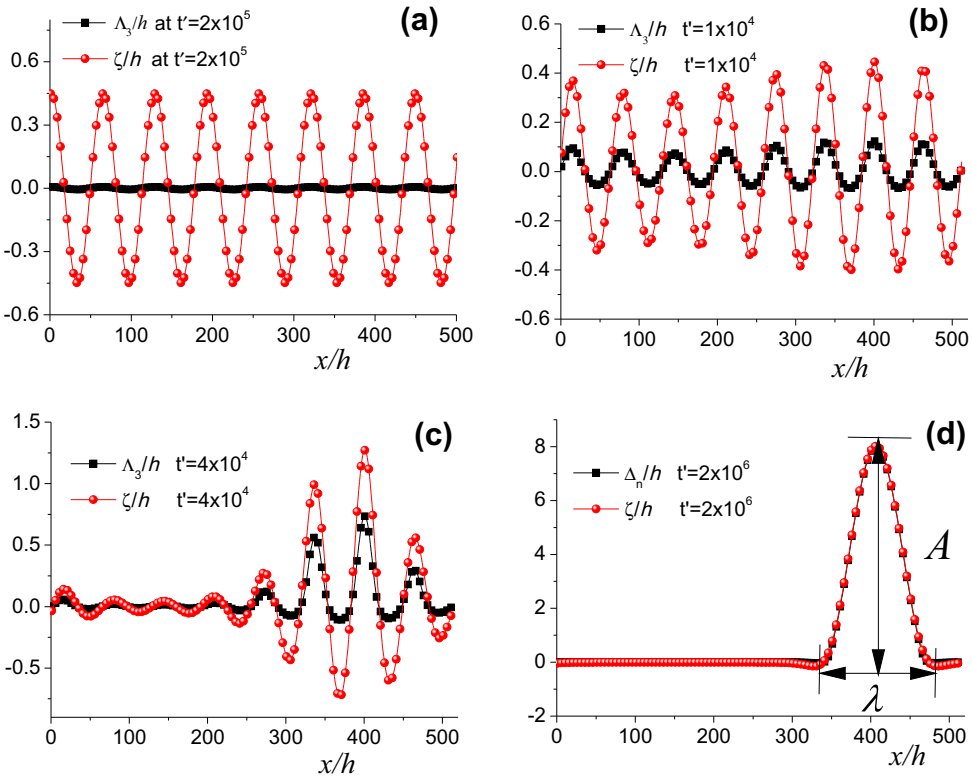

Fig. 3. Numerical simulations of wrinkling and wrinkle-induced delamination under uniaxial compression. The normalized deflection (ζ/h) and normal displacement jump (Λ_3/h) evolve over time in a film/substrate system with $\mu_f/\mu_s = 4200$ and $\varepsilon_{pre} = 0.003$. (a) is for the case of high interfacial toughness with $\gamma_n/\gamma^* = 2.7$, and (b)–(d) are for the case of low interfacial toughness with $\gamma_n/\gamma^* = 0.005$.

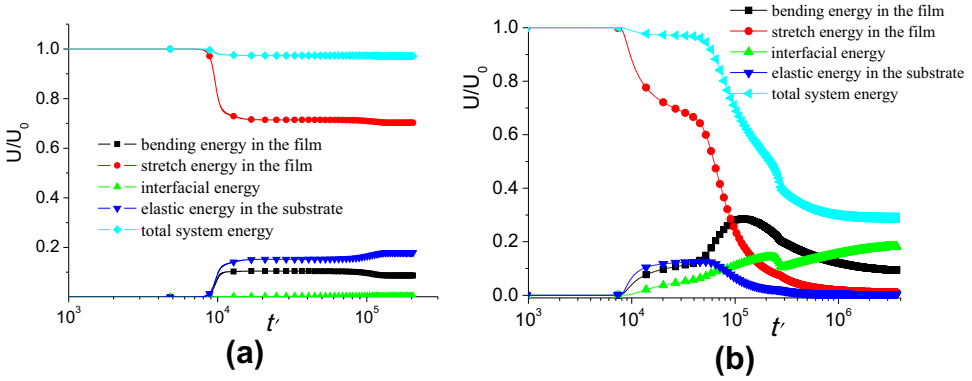

Fig. 4. The simulated energy changes with the normalized time during the development of the buckling instability presented in Fig. 3, (a) for $\gamma_n/\gamma^* = 2.7$, (b) for $\gamma_n/\gamma^* = 0.005$. Here $U_0 = \mu_f h \varepsilon_{pre}^2 S/(1-\nu_f)$ with S the area of the film.

energy contributions. The second stage corresponds to the spontaneous nucleation and growth of the buckle-delamination, with simultaneous decay of the wrinkles (as shown in Fig. 3(c)). In this stage, the stretching energy in the film decreases more rapidly than the first stage while the bending energy increases more rapidly. Moreover, the strain energy of substrate decreases and the potential energy of interface becomes more significant. The third stage is marked by the decrease in the bending energy at $t' > 1 \times 10^5$ due to coarsening of the buckle-delamination till a single straight blister is formed (Fig. 3(d)). Clearly, the total energy relaxation in the processes of wrinkling and wrinkling-induced delamination is largely dominated by reduction of the stretching energy in the film, while the other energy terms (bending, substrate, and interface) increase slightly as a penalty. The potential energy of the interface plays an important role so that further reduction of the stretching energy is hindered by the energetic cost of interfacial delamination in the case of high interfacial toughness ($\gamma_n/\gamma^* = 2.7$), while the stretching energy is significantly reduced after wrinkle-induced delamination for the case of low interfacial toughness ($\gamma_n/\gamma^* = 0.005$).

Growth of wrinkling-induced delamination significantly reduced the compressive stress in the film. For a very compliant substrate (e.g., $\mu_f/\mu_s = 4200$), the stress relaxation extends over a large area, wiping out all the wrinkles (Fig. 3(d)). For a less compliant substrate ($\mu_f/\mu_s = 420$), the stress relaxation is limited to the area around the buckle-delamination blister, while wrinkles remain observable in the area far away from the blister, as shown in Fig. 5(a). The corresponding compressive membrane strain e_{11} plotted in Fig. 5(c) suggests that the relaxation of the elastic membrane strain by the buckle-delamination blister is insufficient to

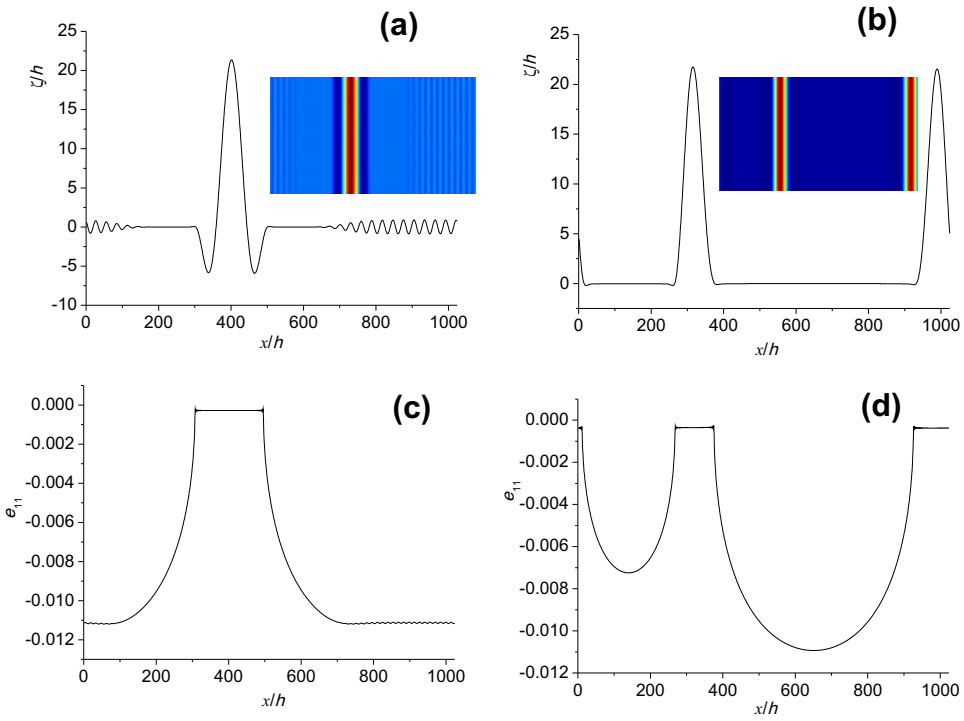

Fig. 5. Transition from concomitant wrinkling and buckle-delamination to an array of buckle-delamination blisters with increasing pre-strain for $\mu_f/\mu_s = 420$ and $\gamma_n/\gamma^* = 0.27$. (a) and (b) are the normalized deflection (ζ/h), for $\varepsilon_{pre} = 0.0275$ and $\varepsilon_{pre} = 0.03$, respectively; (c) and (d) are the corresponding membrane strain component (e_{11}) of the film. The insets show deflection contour patterns of the wrinkles and straight blisters.

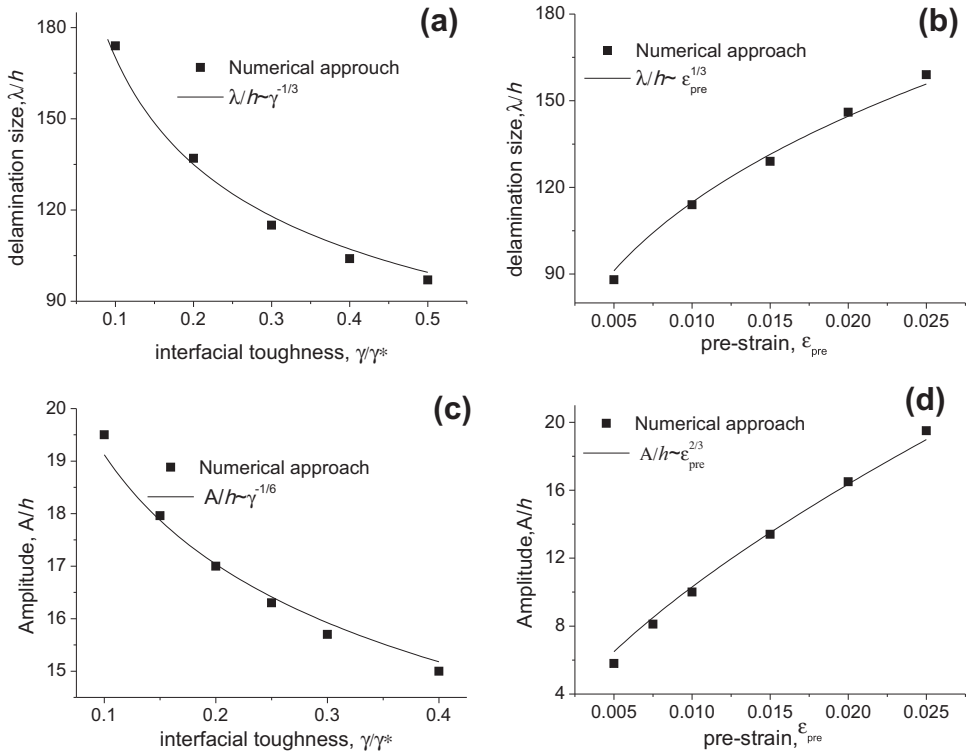

Fig. 6. The calculated buckle amplitude and delamination size of the wrinkling-induced delamination for $\mu_f/\mu_s = 4200$. (a) and (c) as a function of normalized interfacial toughness with $\varepsilon_{pre} = 0.03$; (b) and (d) as a function of pre-strain with $\gamma_n/\gamma^* = 0.054$.

suppress wrinkling far away from the delamination ($\varepsilon_w = 0.0116$). When the pre-strain is further increased, as shown by Fig. 5(b), a second wrinkle-induced delamination blister is formed in the computational domain, with which the compressive membrane strain e_{11} is further relaxed as shown in Fig. 5(d) and hence no wrinkles. The results in Fig. 5 suggest that, subject to increasing

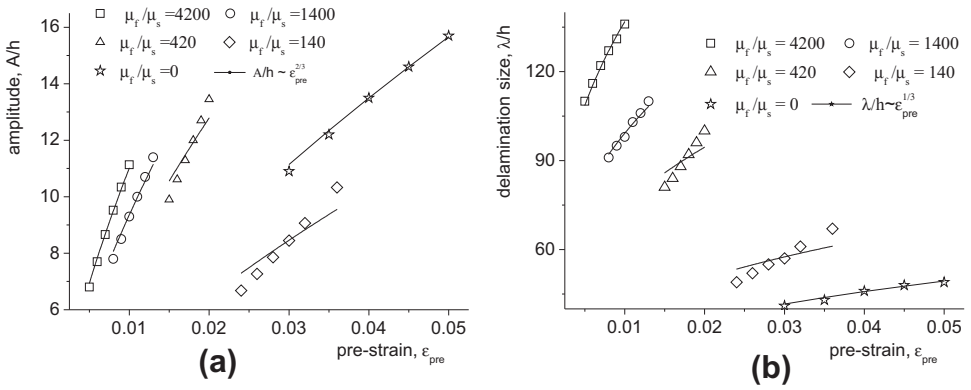

Fig. 7. The calculated buckle amplitude and delamination size of the wrinkling-induced delamination as a function of pre-strain with $\gamma_n/\gamma^* = 0.11$ and different film/substrate modulus ratios.

compressive uniaxial pre-strain, the equilibrium state of the film/substrate system may evolve progressively from flat to wrinkling, to concomitant wrinkles and buckle-delamination, and to an array of parallel buckle-delamination blisters. It is noted that, unlike previous studies on buckle delamination (Chai et al., 1981; Hutchinson et al., 1992; Ortiz and Gioia, 1994; Mei et al., 2011), no pre-existing delamination is assumed in our simulations. While the presence of interfacial defects is practically inevitable in any material systems, the locations and sizes of the pre-existing defects are often unknown, adding uncertainties for the prediction of buckle delamination. For an elastic film on a compliant substrate, wrinkling-induced nucleation of delamination offers an alternative mechanism for the formation of buckle-delamination blisters.

4.3. Equilibrium configuration of straight buckle-delamination blisters

Our numerical simulations show that, without any pre-existing delamination, an elastic film on a compliant substrate develops straight buckle-delamination blisters under uniaxial compression with a relatively large pre-strain as a result of wrinkling-induced delamination. The equilibrium buckling profile of a typical blister is presented in Fig. 3(d), which can be approximately described by a function

$$\zeta = \begin{cases} \frac{A}{2}\left(1+\cos\frac{2\pi x}{\lambda}\right) & -\lambda/2 \leqslant x \leqslant \lambda/2 \\ 0 & \lambda/2 \leqslant |x| \leqslant L/2 \end{cases}, \tag{4.3}$$

where A and λ are the height and width of the blister. In particular, $A = \zeta_{\max} - \zeta_{\min}$ is the difference between the maximum and minimum of the deflection, and λ is taken as the distance between the two points with minimum deflection of the film. In general, the blister profile depends on the pre-strain, the modulus ratio, and interfacial toughness for the film/substrate system, as shown in Fig. 6 for $\mu_f/\mu_s = 4200$. For a fixed pre-strain, both the height and width of the blister decrease as the interfacial toughness increases (Fig. 6(a) and (c)). For a fixed interfacial toughness, both the height and width of the blister increase as the pre-strain increases (Fig. 6(b) and (d)). It is found that the numerical results in Fig. 6 approximately follow a set of power laws, i.e. $A/h \sim \varepsilon_{pre}^{2/3}$, $A/h \sim \gamma_n^{-1/6}$, $\lambda/h \sim \varepsilon_{pre}^{1/3}$, and $\lambda/h \sim \gamma_n^{-1/3}$, as predicted previously by a scaling analysis (Vella et al., 2009). However, for relatively low modulus ratios (e.g., $\mu_f/\mu_s = 420$), the numerical results deviate from the power laws significantly, as shown in Fig. 7. Furthermore, in the limit of a rigid substrate ($\mu_f/\mu_s = 0$), the numerical results again agree with the power laws for both the height and the width.

The limitation of the scaling analysis is revealed by an energetic consideration as follows. The equilibrium profile of the buckle-delamination blister as approximated by Eq. (4.3) may be determined by minimizing the total energy, including the bending energy and stretching energy of the film, the potential energy of the interface, and the elastic strain energy of the substrate:

$$U_{total} = U_s^{film} + U_b^{film} + U_i + U^{sub}. \tag{4.4}$$

For a single straight blister in a square domain with the area $S = L^2$, we obtain

$$U_b^{film} = DL\pi^4 A_{eq}^2/\lambda_{eq}^3, \tag{4.5}$$

$$U_s^{film} = \frac{\mu_f h L^2}{(1-\nu_f)}\left(\frac{\pi^2 A_{eq}^2}{4\lambda_{eq}L} - \varepsilon_{pre}\right)^2, \tag{4.6}$$

$$U_i = \gamma_n \lambda_{eq} L, \tag{4.7}$$

$$U^{sub} = \chi \mu_s \varepsilon_{pre}^2 \lambda_{eq}^2 L \tag{4.8}$$

where χ is a constant characterizing the shape factor of the blister. If the stretch energy in the film and the elastic strain energy of the substrate are negligible, the equilibrium profile of the blister can be determined by a simple balance between the bending energy of the film U_b^{film} and the potential energy of the interface U_i, which would lead to the power laws. We note that the elastic strain energy of the substrate can be negligible only in two extreme cases. First, if the substrate is rigid ($\mu_f/\mu_s = 0$), the deformation of the substrate is zero, thus no energy change in the substrate. Second, if the substrate is very soft ($\mu_f/\mu_s \to \infty$), although the substrate deforms

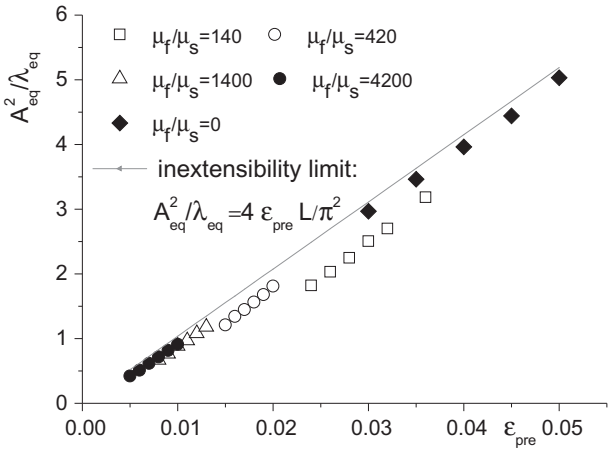

Fig. 8. The calculated geometric relationship of a single buckle-delamination blister with A_{eq}^2/λ_{eq} as a function of pre-strain for different film/substrate modulus ratios, in comparison with the analytical prediction by the condition of inextensibility. Here L is the computational domain size.

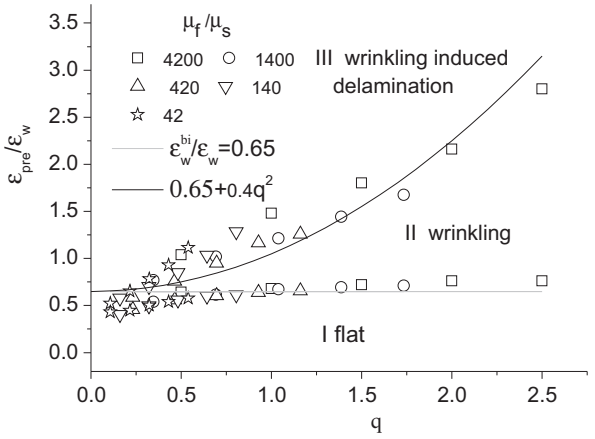

Fig. 9. A phase diagram for wrinkling and delamination in the elastic film/substrate systems under biaxial compression. The open symbols are the critical strains obtained from numerical simulations and the solid lines are fitted by the analytical expressions similar to the case of uniaxial compression.

significantly, the energy change in the substrate is negligibly small due to the small modulus. However, when the modulus ratio is intermediate (e.g., $\mu_f/\mu_s = 420$), the elastic energy change in the substrate becomes an important part of the total energy so that the scaling laws for the blister size would become less accurate. Furthermore, the stretch energy in the film vanishes when the film is assumed to be inextensible so that the height and width of the blister satisfies the condition (Vella et al., 2009)

$$A_{eq}^2/\lambda_{eq} = 4\varepsilon_{pre}L/\pi^2 \tag{4.9}$$

This condition assumes that the membrane strain is fully relaxed everywhere in the film due to the buckle-delamination. Fig. 8 shows the numerical results with A_{eq}^2/λ_{eq} plotted as a function of the pre-strain for different modulus ratios. Apparently, A_{eq}^2/λ_{eq} does increase linearly with pre-strain in all cases. However, while the inextensibility condition in (4.9) is closely followed for very large and very small modulus ratios (e.g., $\mu_f/\mu_s = 4200$ and $\mu_f/\mu_s = 0$), it is not so for intermediate modulus ratios (e.g., $\mu_f/\mu_s = 420$). As shown in Fig. 5, for $\mu_f/\mu_s = 420$, the membrane

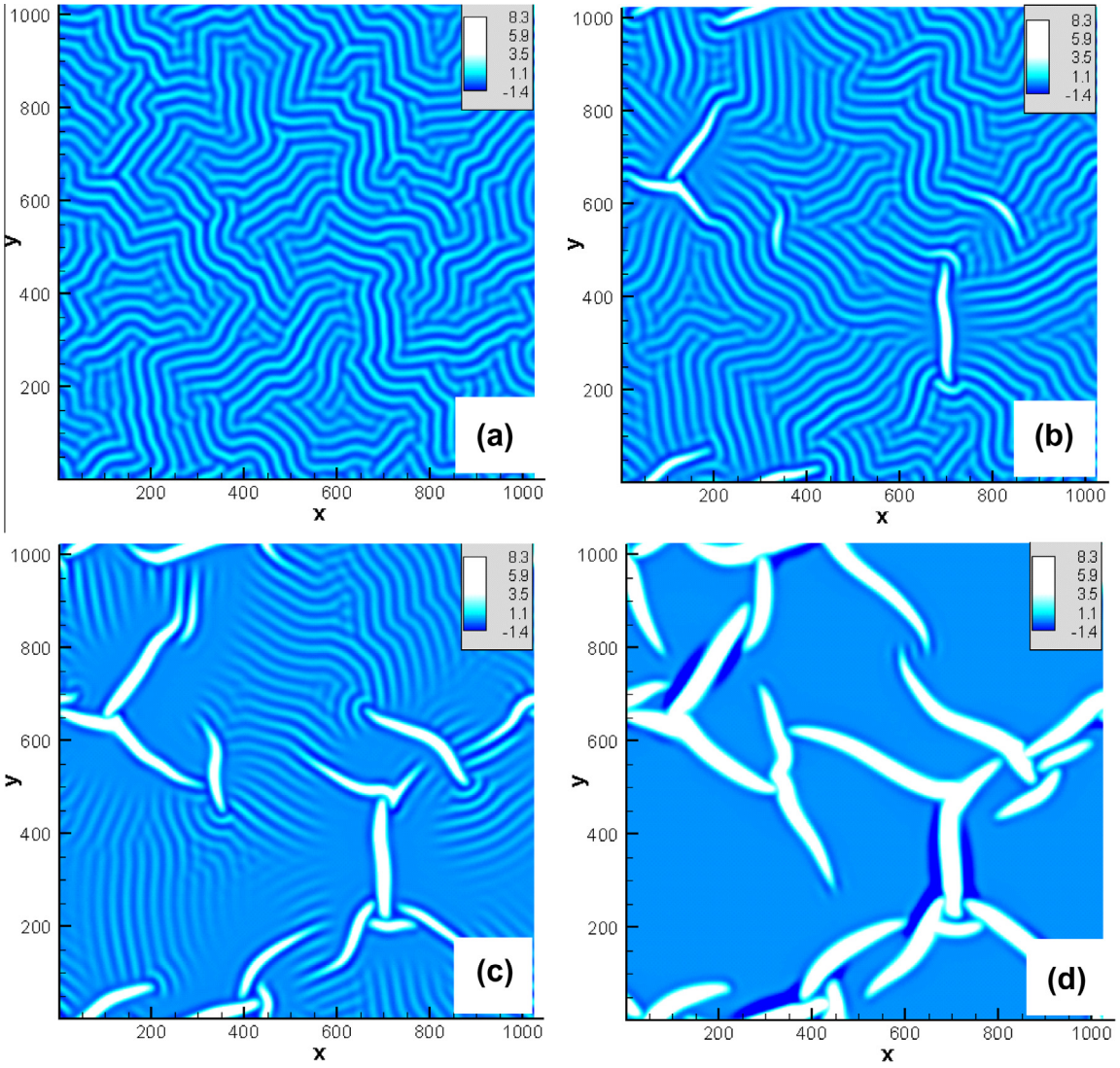

Fig. 10. Simulated evolution of postbuckling morphology from wrinkles to concomitant wrinkling and buckle-delamination and to random buckle-delamination blisters, shown as contours of the normalized deflection (ζ/h) for an elastic film under an equi-biaxial compression with $\varepsilon_{pre} = \varepsilon_{11}^0 = \varepsilon_{22}^0 = 0.0115$ and $\gamma_n/\gamma^* = 0.17$. (a)–(d) for t' = 1000, 4000, 7000, and 40,000.

strain is nearly zero in the delaminated part of the film, but the strain is not fully relaxed in the part bonded to the substrate, consistent with the results in Fig. 8 wherein A_{eq}^2/λ_{eq} is lower than the prediction based on the assumption of inextensibility. Consequently, the numerical results deviate from the scaling laws for the intermediate modulus ratios in Fig. 7. Thus it may be concluded that the scaling laws are most accurate in the two limiting cases with either very large or very small modulus ratios.

4.4. Buckling patterns under biaxial compression

Subject to an equi-biaxial compression, the critical strain for onset of wrinkling instability may be predicted approximately as $\varepsilon_w^{bi} = \frac{\varepsilon_w}{1+\nu_f}$, assuming the same critical stress as the case of uniaxial compression (Huang et al., 2005). The equilibrium wrinkle patterns however are typically chaotic under equi-biaxial compression, depending on the initial conditions and imperfections (Huang and Im, 2006). Consequently, the critical strain for onset of wrinkling-induced delamination cannot be predicted analytically. Following the case of uniaxial compression, we assume a similar form for the critical strain,

$$\varepsilon_{wd}^{bi} = \varepsilon_w^{bi} + B\left[\frac{(3-4\nu_s)\sigma_{\max}}{8(1-\nu_s)\mu_s}\right]^2 \tag{4.10}$$

where B is a dimensionless parameter to be determined numerically. By numerical simulations, we determine the two critical strains for different material parameters (modulus ratio and interfacial toughness) and plot them in Fig. 9 as a phase diagram for the case of equi-biaxial compression, similar to Fig. 2 for uniaxial compression. It is found that the analytical predictions are less accurate under equi-biaxial compression. Nevertheless, the numerical results do collapse onto two curves approximately given by the two equations, $\varepsilon_w^{bi}/\varepsilon_w = \alpha$ and $\varepsilon_{wd}^{bi}/\varepsilon_w = \alpha + Bq^2$ with $\alpha = 0.65$ and $B = 0.4$, respectively. Note that the critical strain for onset of wrinkling is lower than the analytical prediction, i.e., $\alpha < 1/(1+\nu_f)$.

A rich variety of the post-buckling patterns can be obtained under equi-biaxial compression. The phase diagram in Fig. 9 provides a map for selecting the postbuckling patterns from wrinkles to buckle-delamination blisters by varying the pre-strain, the elastic modulus ratio, and the interfacial toughness in numerical simulations. There is a derivation of Eq. (4.10) from numerical results, the reason is possibly due to the fact that the wrinkling profile in

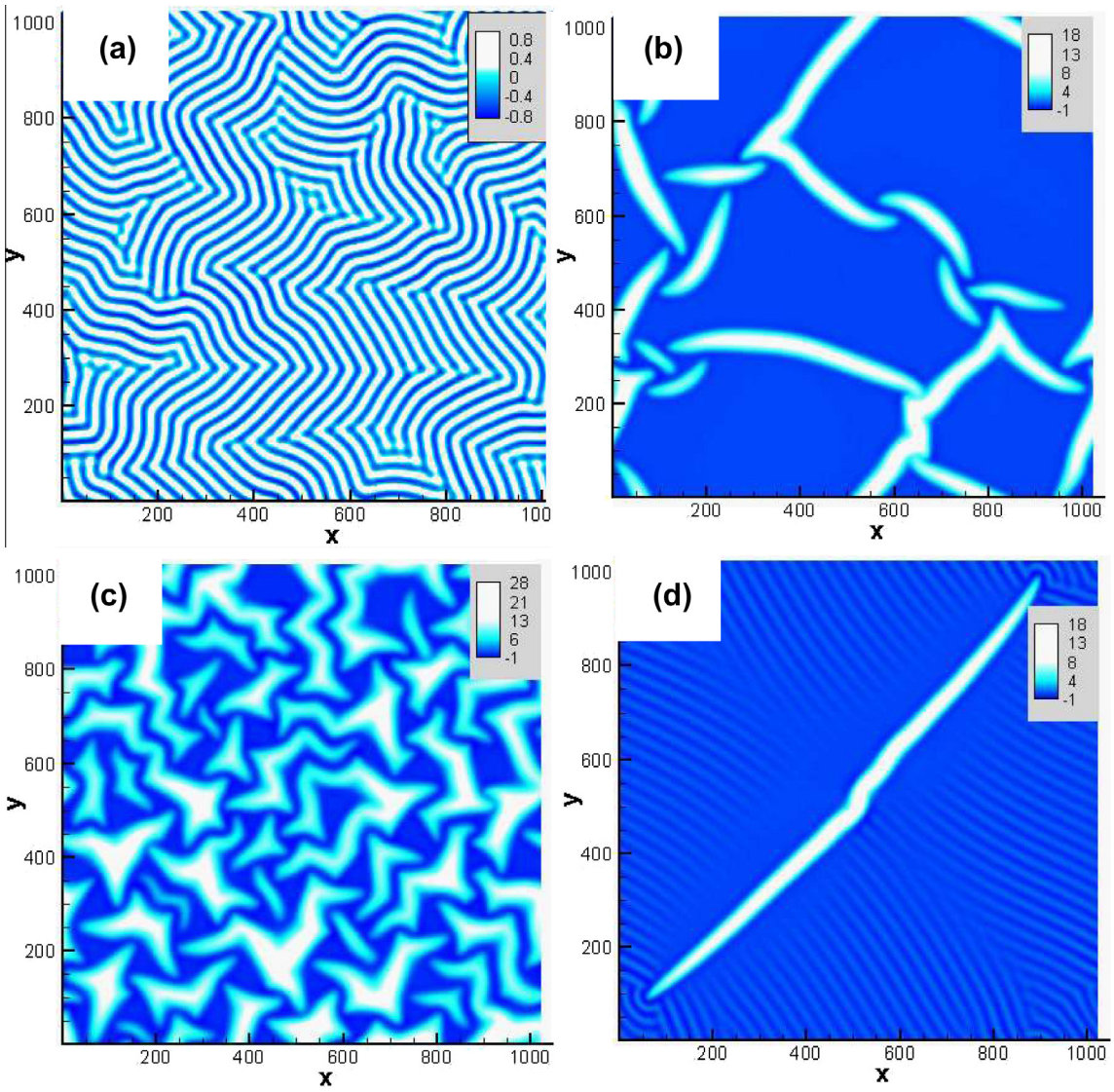

Fig. 11. Simulated post-buckling morphologies of the elastic film/substrate systems: (a)–(c) for increasing pre-strain, $\varepsilon_{pre} = 0.0095$, 0.011, and 0.04, with $\gamma_n/\gamma^* = 0.16$; (d) for $\varepsilon_{pre} = 0.011$ and $\gamma_n/\gamma^* = 0.32$. In all cases, $\mu_f/\mu_s = 420$ and $\gamma_t/\gamma_n = 10$.

the former is assumed to be periodic stripe-like while it could be chessboard-like or randomly-oriented stripes in the latter. As an example, Fig. 10 shows the simulated morphological evolution from wrinkles to buckle-delamination for a film/substrate system with $\mu_f/\mu_s = 4200$ and $\gamma_n/\gamma^* = 0.17$ under an equi-biaxial compression with $\varepsilon_{pre} = \varepsilon^0_{11} = \varepsilon^0_{22} = 0.0115$. Starting from a flat configuration, the film first evolves into a typical labyrinth wrinkle pattern (Fig. 10(a)). Subsequently, multiple buckle-delamination blisters nucleate and grow in different directions (Fig. 10(b)). The buckle-delamination blisters coexist with the wrinkles, as shown in Fig 10(b) and (c). Interestingly, each buckle-delamination blister has a wrinkle depletion area, where the wrinkles tend to be re-aligned in the direction perpendicular to the blister. It is understood that the compressive stress in the film is significantly relaxed around each buckle-delamination blister in the direction perpendicular to blister but not as much in the parallel direction. Therefore, the compressive stress near each blister is nearly uniaxial, resulting in the locally re-aligned wrinkles. Similar surface patterns with coexisting wrinkles and buckle-delamination blisters have been observed experimentally by Mei et al. (2007). Note that this pattern is different from the concomitant wrinkling and buckle-delamination under uniaxial compression (Fig. 5(a)), where the buckle-delamination blister and wrinkles are parallel. As the buckle-delamination grows, after a sufficiently long time, a set of randomly oriented buckle-delamination blisters is obtained, with no wrinkles in between. In this case, the state with coexisting wrinkles and buckle-delamination blisters appear as a transient state, and the equilibrium configuration consists of buckling-delamination blisters only, similar to the experimental observation by Aoyanagi et al. (2010).

There are various buckling patterns observed in experiments for biaxially compressed thin film systems. When the interfacial toughness is high and the pre-strain is in the range, $\varepsilon^{bi}_w < \varepsilon_{pre} < \varepsilon^{bi}_{wd}$, the film only wrinkles and evolves into a herringbone or labyrinth pattern. With lower interfacial toughness or larger pre-strain, wrinkling-induced delamination occurs and develops into buckle-delamination blisters. Fig. 11(a)–(c) shows that, with increasing pre-strain, the equilibrium post-buckling pattern of a film/substrate system changes from herringbone wrinkles to straight buckle-delamination blisters and to blisters with a concave polygon-like shape. Similar patterns have been observed in a carbon film on a glassy substrate (Gioia and Ortiz, 1997). Moreover, the post-buckling pattern depends sensitively on pre-existing defects. Fig. 11(d) shows that, with a pre-existing defect in a 30×60 rectangular area at the center of the computational domain, a straight buckle-delamination blister develops under a relatively small strain and coexists with wrinkles, similar to the experimental observation by Mei et al. (2007). In a separate study (Ni and Soh, 2014), the present model and numerical simulations are employed to study formation of intriguing telephone-cord blisters often observed on relatively stiff substrates. Together, the capability of the present model for simulating complex buckling morphology of elastic thin films is demonstrated.

5. Conclusions

In summary, we have developed a nonlinear continuum model and numerical simulations to investigate the buckling morphological transition from wrinkling to buckle-delamination in thin film structures. The roles of pre-strain, film/substrate modulus ratio, and interfacial toughness are elucidated in the phase diagrams for uniaxial and equi-biaxial compression. In the case of uniaxial compression, parallel wrinkles may develop into straight buckle-delamination blisters through wrinkling-induced delamination. The equilibrium profiles of the buckle-delamination blisters obtained by numerical simulations agree with a set of power laws predicted by a scaling analysis, when the film/substrate modulus ratio is very large or small corresponding to the cases of very soft or rigid substrate, respectively. For the case of equi-biaxial compression, a rich variety of post-buckling patterns are possible. The present model offers a unified approach to study wrinkling and buckle-delamination for diverse thin-film material systems, where the interfacial properties are taken into account explicitly. The numerical method enables simulation of complex buckling patterns comparable to experimental observations. We believe that the unified approach could provide a computational tool for better understanding of diverse buckling patterns in layered material systems, and it could also provide the potential control parameters for manipulating the buckled surface patterns to elaborate the applications wherein tunable surface morphology is favorable.

Acknowledgments

This work was supported by the Basic Research Program of China (Grant No. 2010CB934700, 2011CB302100) and the Chinese Natural Science Foundation (Grant No. 11072232, 11072231, 11132009, 11222219) and the Fundamental Research Funds for the Central Universities (Grant No. WK2090050027). RH gratefully acknowledges financial support by the U.S. National Science Foundation (CMMI-1200161).

References

Abdallah, A.A., Kozodaev, D., Bouten, P.C.P., den Toonder, J.M.J., Schubert, U.S., de With, G., 2006. Buckle morphology of compressed inorganic thin layers on a polymer substrate. Thin Solid Films 503, 167–176.
Aoyanagi, Y., Hure, J., Bico, J., Roman, B., 2010. Random blisters on stickers: metrology through defects. Soft Matter 6, 5720–5728.
Audoly, B., 1999. Stability of straight delamination blisters. Phys. Rev. Lett. 83, 4124–4127.
Audoly, B., Boudaoud, A., 2008. Buckling of a stiff film bound to a compliant substrate. J. Mech. Phys. Solids 56, 2401–2421.
Bowden, N., Brittain, S., Evans, A.G., Hutchinson, J.W., Whitesides, G.M., 1998. Spontaneous formation of ordered structures in thin films of metals supported on an elastomeric polymer. Nature 393, 146–149.
Cai, S., Breid, D., Crosby, A.J., Suo, Z., Hutchinson, J.W., 2011. Periodic patterns and energy states of buckled films on compliant substrates. J. Mech. Phys. Solids. 59, 1094–1114.
Cao, G., Chen, X., Li, C., Ji, A., Cao, Z., 2008. Self-assembled triangular and labyrinth buckling patterns of thin films on spherical substrates. Phys. Rev. Lett. 100, 036102.
Carter, W.C., Taylor, J.E., Cahn, J.W., 1997. Variational methods for microstructural-evolution theories. JOM 49, 30–36.
Chai, H., Babcock, C.D., Knauss, W.G., 1981. One dimensional modeling of failure in laminated plates by delamination buckling. Int. J. Solids Struct. 17, 1069–1083.
Chen, X., Hutchinson, J.W., 2004. Herringbone buckling patterns of compressed thin films on compliant substrates. J. Appl. Mech. 71, 597–603.
Efimenko, K., Rackaitis, M., Manias, E., Vaziri, A., Mahadevan, L., Genzer, J., 2005. Nested self-similar wrinkling patterns in skins. Nat. Mater. 4, 293–297.
Evans, A.G., Mumm, D.R., Hutchinson, J.W., Meier, G.H., Pettit, F.S., 2001. Mechanisms controlling the durability of thermal barrier coatings. Prog. Mater. Sci. 46, 505–553.
Faou, J.Y., Parry, G., Grachev, S., Barthel, E., 2012. How does adhesion induce the formation of telephone cord buckles? Phys. Rev. Lett. 108, 11602.
Freund, L.B., Suresh, S., 2003. Thin Film Materials: Stress, Defect Formation and Surface Evolution. Cambridge University Press, Cambridge, UK.
Genzer, J., Groenewold, J., 2006. Soft matter with hard skin: from skin wrinkles to templating and material characterization. Soft Matter 2, 310–323.
Gioia, G., Ortiz, M., 1997. Delamination of compressed thin films. Adv. Appl. Mech. 33, 119–192.
Goyal, S., Srinivasan, K., Subbarayan, G., Siegmund, T., 2010. On instability-induced debond initiation in thin film systems. Eng. Fract. Mech. 77, 1298–1313.
Groenewold, J., 2001. Wrinkling of plates coupled with soft elastic media. Physica A 298, 32–45.
He, L.H., 2013. Stress and deformation in soft elastic bodies due to intermolecular forces. J. Mech. Phys. Solids 61, 1377–1390.
Huang, R., 2005. Kinetic wrinkling of an elastic film on a viscoelastic substrate. J. Mech. Phys. Solids 53, 63–89.
Huang, R., Im, S.H., 2006. Dynamics of wrinkle growth and coarsening in stressed thin films. Phys. Rev. E 74, 026214.
Huang, Z.Y., Hong, W., Suo, Z., 2004. Evolution of wrinkles in hard films on soft substrates. Phys. Rev. E 70, 030601.

Huang, Z.Y., Hong, W., Suo, Z., 2005. Nonlinear analyses of wrinkles in a film bonded to a compliant substrate. J. Mech. Phys. Solids 53, 2101–2118.
Hutchinson, J.W., Suo, Z., 1992. Mixed-mode cracking in layered materials. Adv. Appl. Mech. 29, 63–191.
Hutchinson, J.W., Thouless, M.D., Liniger, E.G., 1992. Growth and configurational stability of circular, buckling-driven film delaminations. Acta Metall. Mater. 40 (2), 295–308.
Im, S.H., Huang, R., 2008. Wrinkle patterns of anisotropic crystal films on viscoelastic substrates. J. Mech. Phys. Solids 56, 3315–3330.
Jagla, E.A., 2007. Modeling the buckling and delamination of thin films. Phys. Rev. B 75, 085405.
Jiang, H., Khang, D.Y., Song, J., Sun, Y., Huang, Y., Rogers, J.A., 2007. Finite deformation mechanics in buckled thin films on compliant supports. Proc. Natl. Acad. Sci. 104, 15607–15612.
Khang, D.Y., Jiang, H., Huang, Y., Rogers, J.A., 2006. A stretchable form of single-crystal silicon for high-performance electronics on rubber substrates. Science 311, 208.
Lacour, S.P., Jones, J., Wagner, S., Li, T., Suo, Z., 2005. Stretchable interconnects for elastic electronic surfaces. Proc. IEEE 93, 1459–1467.
Mansfield, E.H., 1989. The Bending and Stretching of Plates, second ed. Cambridge Univ. Press, Cambridge, UK.
Mei, H., Huang, R., Chung, J.Y., Stafford, C.M., Yu, H.H., 2007. Buckling modes of elastic thin films on elastic substrates. Appl. Phys. Lett. 90, 151902.
Mei, H., Landis, C.M., Huang, R., 2011. Concomitant wrinkling and buckle-delamination of elastic thin films on compliant substrates. Mech. Mater. 43, 627–642.
Moon, M.W., Jensen, H.M., Hutchinson, J.W., Oh, K.H., Evans, A.G., 2002. The characterization of telephone cord buckling of compressed thin films on substrates. J. Mech. Phys. Solids 50, 2355–2377.
Ni, Y., Soh, A.K., 2014. On the growth of buckle-delamination pattern in compressed anisotropic thin films. Acta Mater. 69, 37–46.
Ni, Y., He, L.H., Liu, Q.H., 2011. Modeling kinetics of diffusion-controlled wrinkles. Phys. Rev. E 84, 051604.
Nilsson, K.F., Giannakopoulos, A.E., 1995. A finite element analysis of configurational stability and finite growth of buckling driven delamination. J. Mech. Phys. Solids 43, 1983–2021.
Ohzono, T., Shimomura, M., 2004. Ordering of microwrinkle patterns by compressive strain. Phys. Rev. B 69, 132202.
Ortiz, M., Gioia, G., 1994. The morphology and folding patterns of buckling-driven thin-film blisters. J. Mech. Phys. Solids 42, 531–559.
Park, K., Paulino, G.H., Roesler, J.R., 2009. A unified potential-based cohesive model of mixed-mode fracture. J. Mech. Phys. Solids 57, 891–908.
Parry, G., Cimetiere, A., Coupeau, C., Colin, J., Grilhe, J., 2006. Stability diagram of unilateral buckling patterns of strip-delaminated films. Phys. Rev. E 74, 066601.
Peyla, P., 2005. Buckling of a compressed elastic membrane: a simple model. Eur. Phys. J. B 48, 379–383.
Stafford, C.M., Harrison, C., Beers, K.L., Karim, A., Amis, E.J., Vanlandingham, M.R., Kim, H.C., Volksen, W., Miller, R.D., Simonyi, E.E., 2004. A buckling-based metrology for measuring the elastic moduli of polymeric thin films. Nat. Mater. 3, 545–550.
Uchida, N., Ohzono, T., 2010. Orientational ordering of buckling-induced microwrinkles on soft substrates. Soft Matter 6, 5729–5735.
van den Bosch, M., Schreurs, P.J.G., Geers, M.G.D., 2006. An improved description of the exponential Xu and Needleman cohesive zone law for mixed-mode decohesion. Eng. Fract. Mech. 73 (9), 1220–1234.
Vandeparre, H., Damman, P., 2008. Wrinkling of stimuloresponsive surfaces: mechanical instability coupled to diffusion. Phys. Rev. Lett. 101, 124301.
Vella, D., Bico, J., Boudaoud, A., Roman, B., Reis, P.M., 2009. The macroscopic delamination of thin films from elastic substrates. Proc. Natl. Acad. Sci. 106, 10901–10906.
Xu, X.P., Needleman, A., 1994. Numerical simulations of fast crack growth in brittle solids. J. Mech. Phys. Solids 42, 1397–1434.
Yang, S., Khare, K., Lin, P.C., 2010. Harnessing surface wrinkle patterns in soft matter. Adv. Funct. Mater. 20, 2550–2564.
Yoo, P.J., Suh, K.Y., Park, S.Y., Lee, H.H., 2002. Physical self-assembly of microstructures by anisotropic buckling. Adv. Mater. 14 (19), 1383–1387.